REDUCED UNCERTAINTIES IN THE FLUTTER ANALYSIS OF THE AEROSTRUCTURES TEST WING

Chan-gi Pak and Shun-fat Lung
NASA Dryden Flight Research Center

Keywords: *aerostructures test wing, flutter margin, structural dynamic model tuning, test validated structural dynamic model, uncertainties*

Abstract

Tuning the finite element model using measured data to minimize the model uncertainties is a challenging task in the area of structural dynamics. A test validated finite element model can provide a reliable flutter analysis to define the flutter placard speed to which the aircraft can be flown prior to flight flutter testing. Minimizing the difference between numerical and experimental results is a type of optimization problem. Through the use of the National Aeronautics and Space Administration Dryden Flight Research Center's (Edwards, California, USA) multidisciplinary design, analysis, and optimization tool to optimize the objective function and constraints; the mass properties, the natural frequencies, and the mode shapes are matched to the target data and the mass matrix orthogonality is retained. The approach in this study has been applied to minimize the model uncertainties for the structural dynamic model of the aerostructures test wing, which was designed, built, and tested at the National Aeronautics and Space Administration Dryden Flight Research Center. A 25-percent change in flutter speed has been shown after reducing the uncertainties.

1 Introduction

A test article called the aerostructures test wing [ATW] was developed and flown at the National Aeronautics and Space Administration [NASA] Dryden Flight Research Center [DFRC] (Edwards, California, USA) on the NF15B (McDonnell Douglas, now The Boeing Company, Chicago, Illinois, USA) test bed aircraft, as shown in figure 1, for the purpose of demonstrating and validating flutter prediction methods during flight [1]. The first aerostructures test wing [ATW1], flown in 2001, was originally developed to directly address requests for better flight flutter test techniques by providing a functional flight test platform. While the first series of tests was extremely successful, the minimum amount of instrumentation (structural accelerometers and strain gages) was chosen to satisfy the scope of the program. These sensors were limited in the capability to answer questions of aeroelastic interactions, sources of nonlinearity, physical mechanisms of aeroelastic coupling, and feedback dynamics between the structure and aerodynamics.

A second aerostructures test wing [ATW2], as shown in figure 2, has been built for the demonstration of state-of-the-art sensor technologies for simultaneous, distributed, and collocated measurement of shear stress (skin friction); steady and unsteady pressures; and structural strain and accelerations for mode shapes and other modal properties. This wing was flown on the NF15B in December 2009.

A block diagram for a robust flutter analysis procedure used at NASA DFRC is given in figure 3. Using a finite element [FE] model for a structural dynamic analysis becomes increasingly important in the modern aircraft design and analysis processes. In general, the quality of an initial FE model of an aircraft is not guaranteed, so we need to perform the ground vibration test [GVT] to validate the FE model. In most cases, these newly built FE models need to be tuned to minimize uncertainties in the structural dynamic FE models and flutter boundary results. Robust flutter analyses performed at NASA DFRC are

mainly based on these validated FE models as shown in figure 3.

Model tuning is a common method to improve the correlation between numerical and experimental modal data, and many techniques have been proposed [2]. Literature reviews on finite element model tuning are summarized in reference [3]. These techniques can be divided into two categories: direct methods (adjust the mass and stiffness matrices directly) and parametric methods (correct the models by changing the structural parameters). The direct methods correct mass and stiffness matrices without taking into account the physical characteristics of the structures and may not be appropriate for use in model tuning processes. In this paper, the tuning method used in the optimization process is the parametric method. In the optimization process, structural parameters are selected as design variables: structural sizing information (thickness, cross sectional area, area moment of inertia, torsional constant, et cetera), point properties (lumped mass, spring constants, et cetera) and materials properties (density, Young's modulus, et cetera). Objective function and constraint equations include mass properties, mass matrix orthogonality, frequencies, and mode shapes. The use of these equations minimizes the difference between numerical results and target data.

The primary objective of this study is to reduce uncertainties in the structural dynamic FE model of the ATW2 to increase the accuracy of flutter speed prediction. Discrepancies are common between the test data and numerical results. However, the FE model can be fine tuned through the use of GVT data. Accurate and reliable GVT results are important to this adjusting process.

The secondary objective of the current study is to add model-tuning capabilities [3] in NASA Dryden's object-oriented multidisciplinary design, analysis and optimization [MDAO] tool [4]. This model tuning technique [3] is essentially based on a non-linear optimization problem.

2 Object-Oriented MDAO Framework

The heart of the object-oriented MDAO tool is the central executive module [CEM] as shown in figure 4. In this module the user will choose an optimization methodology, provide side constraints for continuous as well as discrete design variables and external file names for performance indices; which communicate between the CEM and each analysis module, submit script commands to prepare input data for each analysis code, execute analyses codes, compute performance indices using post-processor codes, and compute an objective function and constraints values from performance indices. The CEM was written in FORTRAN, and script commands for each performance index were submitted through the use of the FORTRAN call system command.

The performance indices for structural optimization problems can include total weight, safety factors, natural frequencies, mode shapes, flutter speed, divergence speed, structural responses at sensor locations, et cetera. On the other hand, the performance indices for the FE model tuning problems can include off-diagonal terms of orthonormalized mass and stiffness matrices, the total error between the measured and computed mode shapes at given sensor points, errors between computed and measured frequencies, total weight, center of gravity [CG] locations, moment of inertia, et cetera.

Two optimization codes are included in the object-oriented MDAO tool: design optimization tools [DOTs] [5] based on a gradient-based algorithm [6] and a genetic algorithm [GA] [7]. The MSC/NASTRAN (MSC Software Corporation, Santa Ana, California, USA), for example, uses a gradient-based approach for optimization [8]. A drawback to this approach is the necessity to compute finite difference or analytical sensitivity values to perform the search, which often requires prior experience based on input defining the problem and search directions.

The DOT is a commercial optimization code that can be used to solve a wide variety of nonlinear optimization problems. When the DOT requires the values of the objective and constraint functions corresponding to a

proposed design, it returns control to the CEM. The CEM calls the DOT again to obtain the next design point. This process is repeated until the DOT returns a parameter to indicate that the optimum objective function is reached. Gradient-based algorithms work well for continuous design variable problems, whereas, GAs can easily handle continuous as well as discrete design variable problems. When there are multiple local minima, GAs are able to find the global optimum results, whereas, gradient-based methods may converge to a locally minimum value.

The GA is directly applicable only to unconstrained optimization so it is necessary to use some additional methods to solve the constrained optimization problem. The most popular approach is to add penalty functions, in proportion to the magnitude of the constraint violation, to the objective function [9].

The general form of the exterior penalty function is shown in equation (1):

$$\mathbf{L}(\bar{\mathbf{X}}) = \mathbf{F}(\bar{\mathbf{X}}) + \sum_{i=1}^{q} \lambda_i \mathbf{g}_i(\bar{\mathbf{X}}) + \sum_{j=1}^{r} \lambda_{j+q} \mathbf{h}_j(\bar{\mathbf{X}}) \qquad (1)$$

where $\mathbf{L}(\bar{\mathbf{X}})$ indicates the new objective function to be optimized, $\mathbf{F}(\bar{\mathbf{X}})$ is the original objective function, $\mathbf{g}_i(\bar{\mathbf{X}})$ is the inequality constraint, $\mathbf{h}_j(\bar{\mathbf{X}})$ is the equality constraint, λ_i are the scaling factors, $\bar{\mathbf{X}}$ is the design variables vector, and q and r are the number of inequality and equality constraints, respectively.

Five optimization methodologies available in the CEM are described as follows:

- Genetic algorithm with continuous, discrete or mixed (continuous/discrete) design variables [GCD];
- Gradient-based algorithm, that is DOT, with continuous design variables [DC];
- Start with GCD then continue with DC;
- Start with GCD then continue with DC then continue with genetic algorithm with discrete design variables [GD]; and
- Start with DC then continue with GD.

3 Structural Dynamic Model Tuning Procedure

Discrepancies in frequencies and mode shapes are minimized using a series of optimization procedures [3, 10, 11]. The numerical mass properties, the mass matrix orthogonality, and the natural frequencies and mode shapes are matched to the target values based on the following three tuning steps.

3.1 Step 1: Tuning Mass Properties

The difference in the numerical and target values of the total mass, the center of gravity [CG] location, and mass moment of inertias at the CG location are used as performance indices. The resulting 10 performance indices, as shown in equations (2) through (11), are defined to minimize the uncertainties in the rigid body dynamics.

$$\mathbf{J_1} = (\mathbf{W} - \mathbf{W}_G)^2 / \mathbf{W}_G^2 \qquad \textbf{(Total weight)} \qquad (2)$$

$$\mathbf{J_2} = (\mathbf{X} - \mathbf{X}_G)^2 / \mathbf{X}_G^2 \qquad \textbf{(X-CG)} \qquad (3)$$

$$\mathbf{J_3} = (\mathbf{Y} - \mathbf{Y}_G)^2 / \mathbf{Y}_G^2 \qquad \textbf{(Y-CG)} \qquad (4)$$

$$\mathbf{J_4} = (\mathbf{Z} - \mathbf{Z}_G)^2 / \mathbf{Z}_G^2 \qquad \textbf{(Z-CG)} \qquad (5)$$

$$\mathbf{J_5} = (\mathbf{I_{XX}} - \mathbf{I_{XXG}})^2 / \mathbf{I}_{\mathbf{XXG}}^2 \qquad \textbf{(Ixx at CG location)} \qquad (6)$$

$$\mathbf{J_6} = (\mathbf{I_{YY}} - \mathbf{I_{YYG}})^2 / \mathbf{I}_{\mathbf{YYG}}^2 \qquad \textbf{(Iyy at CG location)} \qquad (7)$$

$$\mathbf{J_7} = (\mathbf{I_{ZZ}} - \mathbf{I_{ZZG}})^2 / \mathbf{I}_{\mathbf{ZZG}}^2 \qquad \textbf{(Izz at CG location)} \qquad (8)$$

$$\mathbf{J_8} = (\mathbf{I_{XY}} - \mathbf{I_{XYG}})^2 / \mathbf{I}_{\mathbf{XYG}}^2 \qquad \textbf{(Ixy at CG location)} \qquad (9)$$

$$\mathbf{J_9} = (\mathbf{I_{YZ}} - \mathbf{I_{YZG}})^2 / \mathbf{I}_{\mathbf{YZG}}^2 \qquad \textbf{(Iyz at CG location)} \qquad (10)$$

$$\mathbf{J_{10}} = (\mathbf{I_{ZX}} - \mathbf{I_{ZXG}})^2 / \mathbf{I}_{\mathbf{ZXG}}^2 \qquad \textbf{(Izx at CG location)} \qquad (11)$$

In the case of a DOT optimization, it is recommended to start an optimization procedure at a feasible domain. When the optimization procedure starts in an infeasible domain, there is

no guarantee that the design will move to a feasible domain. To this end, these ten sub-optimization criteria are used (if test data is available) to make a feasible starting configuration for the second and the third optimization steps.

The exterior penalty function approach given in equation (1) is used for the GA optimization. For example, the performance index $\mathbf{J_1}$ and performance indices $\mathbf{J_2}$ through $\mathbf{J_{10}}$ can be selected as an objective function and constraints, respectively. Therefore, the following objective function, J, can be used for the GA optimization as shown in equation (12):

$$J = J_1 + \sum_{i=2}^{10} \lambda_i J_i \tag{12}$$

where λ_i is the scaling factors and $i = 2,\ldots, 10$.

3.2 Step 2: Tuning Mass Matrix

The off-diagonal terms of the orthonormalized mass matrix are reduced to improve the mass orthogonality as shown in equation (13):

$$\mathbf{J}_{11} = \sum_{i=1, j=1, i\neq j}^{n} \left(\overline{\mathbf{M}}_{ij}\right)^2 \tag{13}$$

where n is the number of modes to be matched and $\overline{\mathbf{M}}$ is defined as shown in equation (14).

$$\overline{\mathbf{M}} = \Phi_G^T \mathbf{T}^T \mathbf{M} \mathbf{T} \Phi_G \tag{14}$$

The performance index $\mathbf{J}_{11}$ is used as the objective function, and performance indices $\mathbf{J}_1$ through $\mathbf{J}_{10}$ are used as constraints in this step. In equation (14), the mass matrix $\mathbf{M}$ is calculated from the FE model while the target eigen-matrix Φ_G is measured from the GVT. The eigen-matrix Φ_G remains constant during the optimization procedure. A transformation matrix $\mathbf{T}$ [3] in equation (14) is based on Guyan reduction, improved reduction system [12] or system equivalent reduction expansion process [SEREP] [13]. This reduction is required due to the limited number of available sensor locations and difficulties in measuring the rotational DOFs.

3.3 Step 3: Tuning Frequencies and Mode Shapes

Two options can be used for tuning the frequencies and mode shapes. In the first option, the objective function considered combines a performance index $\mathbf{J}_{12}$ (the normalized errors between GVT and computed frequencies) as shown in equation (15) with a performance index $\mathbf{J}_{13}$ (the total error associated with the off-diagonal terms of the orthonormalized stiffness matrix) as shown in equation (16).

$$\mathbf{J}_{12} = \sum_{i=1}^{n} \left(\frac{\Omega_i - \Omega_{iG}}{\Omega_i} \right)^2 \tag{15}$$

$$\mathbf{J}_{13} = \sum_{i=1, j=1, i\neq j}^{n} \left(\bar{\mathbf{K}}_{ij}\right)^2 \qquad \textbf{(option 1)} \tag{16}$$

The matrix $\bar{\mathbf{K}}$ is obtained from the following matrix products as shown in equation (17):

$$\bar{\mathbf{K}} = \Phi_G^T T^T \mathbf{K} \mathbf{T} \Phi_G \tag{17}$$

where the stiffness matrix, $\mathbf{K}$, is calculated from the FE model.

In the second option, the objective function considered combines the performance index $\mathbf{J}_{12}$ with a new performance index $\mathbf{J}_{13}$ (the total error between GVT and computed mode shapes at given sensor points) as shown in equation 18.

$$\mathbf{J}_{13} = \sum_{i=1}^{m} \sum_{j=1}^{n} \left(\Phi_{ij} - \Phi_{ijG}\right)^2 \qquad \textbf{(option 2)} \tag{18}$$

The performance index $\mathbf{J}_{13}$, in the second option, is much simpler than in the first option for this application. Any errors in both the modal frequencies and the mode shapes are minimized by including an index for each of these in the objective function. For the second option, a small number of sensor locations can

be used at which errors between the GVT and computed mode shapes are obtained.

Instead of using the summation in equations (13) and (15), each individual term can be a separate performance index. In this case, the total number of performance indices for steps 2 and 3 will increase, however, it is easier to apply the military standard requirements.

Any one or combinations of performance indices $\mathbf{J}_1$ through $\mathbf{J}_{13}$ can be used as the objective function with the other performance indices treated as constraints. This gives the flexibility to achieve the particular optimization goal while maintaining the other properties as close to the desired target value as possible. The optimization problem statement can be written as

Minimize J_i
Such that $J_k \leq \varepsilon_k$, for $k = 1$ through 13 and $k \neq i$

where ε_k is a small value that can be adjusted according to the tolerance of each constraint condition.

4 Test Article

The ATW2 was used to demonstrate NASA Dryden's object-oriented MDAO tool through the process of ground vibration testing and the model tuning technique. This test article was a small-scale airplane wing comprised of an airfoil and wing tip boom as shown in figure 5. The major structural component was the composite wing spar with a rectangular cross section. This wing had equally spaced four ribs and composite upper and lower cover skins. The empty space between the upper and the lower cover skins was filled with plastic foam. This wing was based on a NACA-65A004 airfoil shape with a 3.28 aspect ratio. The wing had a half span of 18 in (45.720 cm) with a root chord length of 13.2 in (33.528 cm) and a tip chord length of 8.7 in (22.098 cm). The total area of this wing was 197 in^2 (1270.965 cm^2). The wing tip boom was a 1-in (2.540 cm) diameter hollow tube of 21.5 in (54.610 cm) in length. The total weight of the wing was 2.66 lb (0.9928 kg).

Since the ATW2 was attached to the NF15B flight test fixture, the construction of the wing was limited to lightweight materials with no metal for the safety of re-contact with the aircraft after a possible separation. The wing and spar were constructed from fiberglass cloth, the tip boom used carbon fiber composite, the wing core consisted of rigid foam, and the components were attached by epoxy. The wing skin was made of three plies of fiberglass cloth with a 0.01-in (0.254 mm) thickness. The internal spar located at the 30-percent chord line was composed of 10 plies with a 0.05-in (1.270-mm) thickness of carbon at the root, and decreasing to 1 ply 0.005-in (0.127 mm) thickness at the tip.

5 Test Setup

Ground vibration tests were performed to determine the dynamic modal characteristics of the ATW2. In the test set up, the ATW2 was clamped on to a circular aluminum plate, which was bolted to a mounting panel, and then installed into a small strong back called the ground test fixture in the NASA Dryden Flight Loads Laboratory. The PONTOS photogrammetry optical measuring system (Gesellschaft für Optische Messtechnik, Braunschweig, Germany) [14], as shown in figure 6, was used to measure output displacement at the sensor points, shown in figure 7. For the excitation method, an impulse hammer with an impedance head was used to excite the ATW2's natural frequencies and mode shapes as well as to measure input forces.

PONTOS is a non-contact optical 3D measuring system. It analyzes, computes, and documents object deformations, rigid body movements, and the dynamic behavior of a measuring point [14]. The PONTOS system provides an alternative for complex sensor technology like laser sensor, draw-wire sensors, or accelerometers, which are commonly used in the GVT for measuring responses of the structure. The features of the PONTOS system include:

- an unlimited number of sensors (The sensor markers are extremely

lightweight so that a large number of sensors can be used at the same time without essentially altering the total weight or the mode shapes of the structure.),

- non-contact acquisition of the precise 3D position of any number of measuring points,
- mobility and flexibility due to an easy and compact measuring system, and
- easy and quick adaptation to different measuring volumes and measuring tasks.

The limitations of the PONTOS system include:

- measuring frame rate up to 500 Hz at 1280x1024 pixels,
- measuring volume up to 1700 by 1360 by 1360 mm^3, and use on a plane or a slightly curved surface.

6 Flutter Analysis Before Model Tuning

Natural frequencies obtained from the GVT and the MSC/NASTRAN modal analyses using FE models before model tuning are compared in table 1. The starting configuration of the FE model was obtained from the ATW1 model. The GVT frequencies in this table were based on the time history responses data, as shown in figure 8, collected by the PONTOS system at each of the sensor points. The eigensystem realization algorithm routine, which was developed by Juang and Pappa [15] at NASA Langley Research Center, was then used to identify the frequencies and mode shapes of the system. The FE model for the MSC/NASTRAN [16] modal analysis is shown in figure 9. Detailed GVT sensor locations and GVT mode shapes are provided in reference [17]. Corresponding natural frequencies and mode shapes computed using the MSC/NASTRAN code are shown in figure 10. In table 1 and figure 10, the mode numbers 1, 2, and 3 are the first bending, first torsion, and second bending modes, respectively.

A matched flutter analysis of the ATW2 using the ZAERO code [18] is presented in this section. The first 10 natural modes were used for the flutter analysis. The aerodynamic model has 200 surface elements on the wing and 216 body elements on the boom. Forty-four splining points were used between the structural dynamic and aerodynamic models. The aerodynamic model of the ATW2 and the first three splined mode shapes on the aerodynamic model are shown in figures 11 and 12, respectively. The matched flutter analyses were performed at Mach 0.60, 0.75, 0.82 and 0.95. The aerodynamic influence coefficient matrices at each Mach number were generated at 16 reduced frequencies and the *g*-method [18] was used in the matched flutter analysis.

The speed versus damping, V-g, and speed versus frequency, V-w, curves from the matched flutter analysis at Mach 0.82 (the ATW1 flutter Mach number) [1] before model tuning are given in figure 13. The structural damping used for the flutter speed computation was 3 percent. The flutter speed was 407.4 KEAS, flutter frequency was 22.86 Hz, and the corresponding altitude was 15,010 ft (4,575 m), as shown in table 2.

Modal participation factors for the first flutter mode are given in table 3. Modal participation of the first three natural frequencies was more than 96 percent before model tuning. In-plane modes, mode numbers 4, 6, and 8, did not contribute to the first flutter mode. In table 3, we can conclude that the primary structural dynamic modes for the first flutter mode were modes 1, 2 and 3 and the secondary modes for the first flutter mode were modes 5, 7, 9 and 10. The first mode is the dominant mode for the primary flutter mode.

7 Model Tuning

Based on military standards [19, 20], the frequency error should be less than 3 percent for the primary modes and 10 percent for the secondary modes. Using a norm of frequency differences as an objective function with mass properties, mass orthogonality, and mode shapes as constraint equations, the frequencies after model tuning are presented in table 1. Before model tuning the frequency error for the second mode was 47.3 percent and the frequency error for the third mode was 11.9 percent. These frequency errors violate the 3-percent frequency

error requirements in military standards. After model tuning the 2.09-percent error becomes 3.19 percent, the 47.3-percent error becomes 1.38 percent, and the 11.9-percent error becomes 0.39 percent. After model tuning, 3 percent frequency error requirements for the primary modes were satisfied for modes 2 and 3, and close to being satisfied for mode 1.

Since Guyan reduction is a static condensation, it is only accurate for lower modes. For higher modes, the errors become too large as shown in table 1. Unlike Guyan reduction, the SEREP preserves the dynamic character of the original full system model for selected modes of interest. The dynamic characteristics of the reduced model were virtually the same as the full model as shown in table 1. Therefore, the SEREP model reduction process was chosen for this ATW2 model update application.

Table 4 shows the total weight, orthonormalized mass matrix, and modal assurance criterion [MAC] [3] values of the ATW2 before and after model tuning. Based on military standards, the off-diagonal terms of the orthonormalized mass matrix should be less than 10 percent [19, 20]. The off-diagonal terms of the orthonormalized mass matrix, with a maximum of 38 percent before model tuning, are minimized in the second tuning step. The maximum off-diagonal term of 7.43 percent after model tuning is observed in table 4 and satisfies the 10-percent limitation in military standards. Model correlation with test data prior to model tuning was poor and unacceptable to proceed to flight. The MAC values of 0.70 and 0.75 for modes 2 and 3 before model tuning become 0.97 and 0.95, respectively. Therefore, we can conclude that excellent model correlation with the test data was achieved after model tuning, which leads to a more reliable flutter speed prediction.

8 Flutter Analysis After Model Tuning

Typical V-g and V-w curves from the matched flutter analysis at Mach 0.82 after model tuning are given in figure 14. The same 3-percent structural-damping value is used for flutter speed computation. In figure 14 we can observe a steeper merging behavior for the first bending and torsion modes after model tuning. It is important for the safety of flight that the model tuning results predict a more sudden, rather than a more gradual, flutter onset.

The results of the matched flutter analysis before and after model tuning are summarized in tables 2 and 5. The modal participation factors in table 5 indicate that the first three modes have more than a 95-percent contribution to the first flutter mode before model tuning and more than a 98-percent contribution after model tuning. The second mode, which has the maximum frequency difference before model tuning as shown in table 1, becomes more than 91 percent of the modal participation after model tuning at Mach 0.60. Therefore, the second mode after tuning becomes the dominant mode for the primary flutter mode. The resulting flutter speed difference due to model uncertainty was also a maximum at Mach 0.60, as shown in table 2. Table 2 shows that the flutter speed difference varies from 25.4 percent at Mach 0.60 to 3.0 percent at Mach 0.95. As shown in tables 2 and 5 after model tuning, the modal participation of the second mode, which is the dominant mode, decreased when Mach number increased; the differences in flutter speed due to uncertainty also decreased when Mach number increased.

Finally, flutter boundaries of the ATW2, before and after model tuning, are compared with the flight envelopes as shown in figure 15. The solid and long dash dotted lines are the flight envelope of the mother ship and its 15-percent margin, respectively. The dashed line represents the ATW 2 test envelope that is planned for flight, and the long dash double dot line is the 15-percent margin of the ATW2 test envelope. The solid line with the square marker is the flutter boundary before model tuning and the solid line with the diamond marker represents flutter boundary after model tuning. It should be noted that flutter boundary after model tuning is more conservative than before model tuning.

9 Concluding Remarks

This paper describes the reduced uncertainty procedures for the ATW2, which was developed at the NASA Dryden Flight Research Center for demonstrating flutter and advanced aeroelastic test techniques. It has been shown that model uncertainties can be reduced through the tuning of the finite element model using the NASA DFRC's object-oriented MDAO tool.

After tuning the FE model, the frequency differences between GVT and analytical results are mostly within 3 percent and the off-diagonal terms of the orthonormalized mass matrix are within 10 percent satisfying the military standards. Excellent mode shape correlations were also achieved through the high MAC value (greater than 95 percent). With the updated FE model, the flutter speed prediction can be reduced as much as 25 percent at Mach 0.60.

Acknowledgement

This object-oriented multidisciplinary design, analysis, and optimization tool development was supported mainly by the Aeronautics Research Mission Directorate Subsonic Fixed Wing project and partly by the Aeronautics Research Mission Directorate Supersonics project under the Fundamental Aeronautics program.

References

[1] Lind R, Voracek D, Truax R, Doyle T, Potter S and Brenner M. A flight test to demonstrate flutter and evaluate flutterometer. *The Aeronautical Journal*, Vol. 107, No. 1076, pp 577 – 588, October 2003.

[2] Friswell M and Mottershead J. *Finite element model updating in structural dynamics*. Kluwer Academic Publishers, 1995.

[3] Pak C. Finite element model tuning using measured mass properties and ground vibration test data. *ASME Journal of Vibration and Acoustics*, Vol. 131, Issue 1, February 2009.

[4] Pak C and Li W. Multidisciplinary design, analysis and optimization tool development using a genetic algorithm**.** *Proceedings of the 26th Congress of International Council of the Aeronautical Science*, Anchorage, Alaska, 2008.

[5] *DOT design optimization tools user's manual version 5.0*. Vanderplaats Research & Development, Inc., 2001.

[6] Vanderplaats G. *Numerical optimization techniques for engineering design*, 3rd Edition, Vanderplaats Research & Development, Inc., 2001.

[7] Charbonneau P and Knapp B. *A user's guide to PIKAIA 1.0*, National Center for Atmospheric Research, 1995.

[8] EI-Borgi S, Neifar M, Cherif F, Choura S and Smaoui H. Modal identification, model updating and nonlinear analysis of a reinforced concrete bridge. *Journal of Vibration and Control*, Vol. 14, No. 4, pp. 511-530, 2008.

[9] Yeniay Ö. Penalty function methods for constrained optimization using genetic algorithms. *Mathematical and Computational Applications*, Vol. 10, No. 1, pp. 45-56, 2005.

[10] Lung S and Pak C. Structural model tuning capability in an object-oriented multidisciplinary design, analysis and optimization tool. *Proceedings of the 26th Congress of International Council of the Aeronautical Sciences*, Anchorage, Alaska, 2008.

[11] Herrera C and Pak C. Build-up approach to updating the mock quiet spike beam model. AIAA-2007-1776, *Proceedings of the 48th AIAA/ASME/ASCE/AHS/ASC Structures, Structural Dynamics, and Materials Conference*, Honolulu, Hawaii, April 23-26, 2007.

[12] O'Callahan J. A procedure for an improved reduced system (IRS) model. *Proceedings of the 7th International Modal Analysis Conference*, Las Vegas, Nevada, Vol. 1, pp. 17-21, 1989.

[13] O'Callahan J, Avitabile P and Riemer R. System equivalent reduction expansion process. *Proceedings of the 7th International Modal Analysis Conference*, Las Vegas, Nevada, Vol. 1, pp. 29-37, 1989.

[14] *Pontos user manual version 6.0*. Gesellschaft für Optische Messtechnik, 2007.

[15] Juang J and Pappa R. An eigensystem realization algorithm for modal parameter identification and modal reduction. *AIAA Journal of Guidance, Control, and Dynamics*, Vol. 8, No. 5, pp. 620-627, 1984.

[16] *MSC/NASTRAN quick reference guide version 69*. The MacNeal Schwendler Corporation, 2005.

[17] Lung S and Pak C. Updating finite element model of the aerostructures test wing with ground vibration test data. NASA TM-2009-214646, April 2009.

[18] *ZAERO user's manual version 8.2*. ZONA Technology, Inc., October 2008.

[19] Military Standard. Test requirements for launch, upper-stage, and space vehicles. MIL-STD-1540C Section 6.2.10, September 15, 1994.

[20] Norton W. Structures flight test handbook. AFFTC-TIH-90-001, November 1990.

Tables

Table 1. Natural frequencies of the ATW2 before and after model tuning.

Mode	GVT (Hz)	Before tuning		After tuning	
		MSC/NASTRAN (Guyan/full; Hz)	Error (%)	MSC/NASTRAN (SEREP/full; Hz)	Error (%)
1	17.24	17.61/17.60	2.15/ 2.09	17.79/17.79	3.19/ 3.19
2	44.10	23.27/23.26	-47.20/ -47.30	44.71/44.71	1.38/ 1.38
3	84.00	99.02/93.99	17.90/ 11.90	84.33/84.33	0.39/ 0.39

Table 2. Flutter boundaries before and after model tuning.

		Mach = 0.60	Mach = 0.75	Mach = 0.82	Mach = 0.95
Before tuning	Speed, KEAS	453.0	421.5	407.4	377.9
	Frequency, Hz	23.18	22.97	22.86	22.53
	Altitude, ft	-7,501	8,751	15,010	25,590
After tuning	Speed, KEAS	361.3	364.6	365.3	367.0
	Frequency, Hz	38.47	37.73	37.32	36.20
	Altitude, ft	5,101	16,080	20,310	26,920
Speed difference, percent		25.4	15.6	11.5	3.0

Table 3. Modal participation factors at Mach 0.82 before model tuning.

Mode	Frequency, Hz	Modal participation factor, percent	
1	17.60	75.0	
2	23.26	16.8	96.6*
3	93.99	4.8	
4	135.40	0.0	
5	163.10	2.6	
6	174.50	0.0	
7	257.50	0.5	3.4**
8	391.60	0.0	
9	394.30	0.1	
10	445.60	0.3	

*: The total of the first three modes
**: The total of modes 5, 7, 9 and 10

Table 4. Summary of total weight, orthonormalized mass matrix, and MAC values for the ATW2 before and after model tuning.

		Measured	Before tuning			After tuning		
Total weight		2.66 lb	1.76 lb (error 34%)			2.72 lb (error 2.3%)		
Orthonormalized mass matrix			1	2	3	1	2	3
	1		1.0000	-0.2490	0.3800	1.0000	0.0395	-0.0565
	2		-0.2490	1.0000	-0.6610	0.0395	1.0000	-0.0743
	3		0.3800	-0.6610	1.0000	-0.0565	-0.0743	1.0000
Modal assurance criteria	Mode 1		0.97			0.99		
	Mode 2		0.70			0.97		
	Mode 3		0.75			0.95		

Table 5. Modal participation factors before and after model tuning.

Mode	Frequency, Hz	Modal participation factors before model tuning, percent							
		Mach = 0.60		Mach = 0.75		Mach = 0.82		Mach = 0.95	
1	17.60	68.1		72.9		75.0		79.7	
2	23.26	22.2	95.5*	18.3	96.2*	16.8	96.6*	13.6	97.6*
3	93.99	5.2		5.0		4.8		4.3	
Mode	Frequency, Hz	Modal participation factors after model tuning, percent							
		Mach = 0.60		Mach = 0.75		Mach = 0.82		Mach = 0.95	
1	17.79	6.7		9.8		12.3		24.3	
2	44.71	91.9	99.2*	88.4	99.1*	85.6	99.0*	72.4	98.3*
3	84.33	0.6		0.9		1.1		1.6	

*: These are the sum of modes 1, 2 and 3 for each Mach number.

Figures

Fig. 1. The aerostructures test wing mounted on the NF-15B for flight flutter testing.

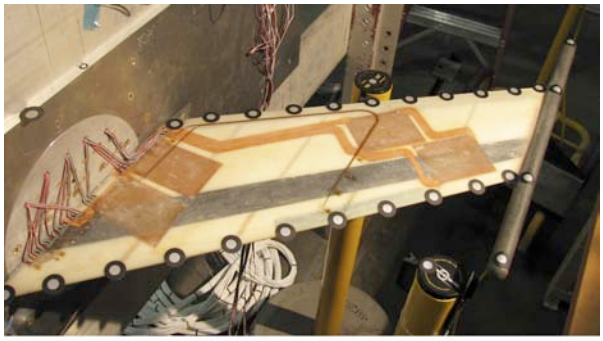

Fig. 2. The aerostructures test wing 2.

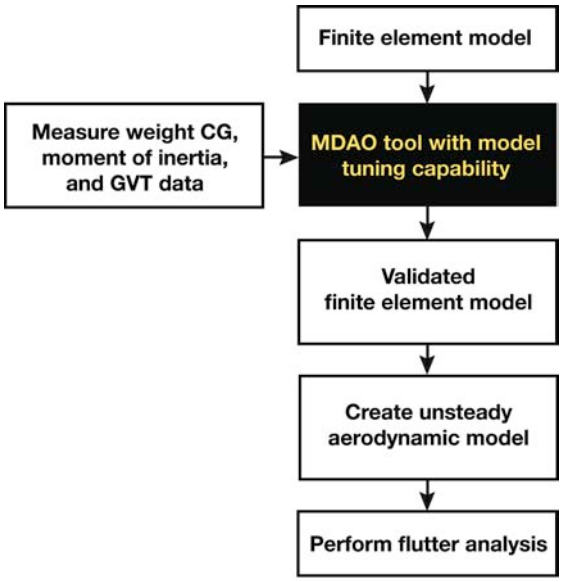

Fig. 3. Robust flutter analysis procedure at NASA DFRC.

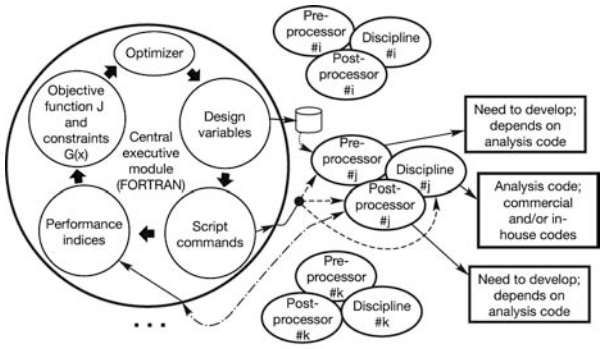

Fig. 4. Central executive module.

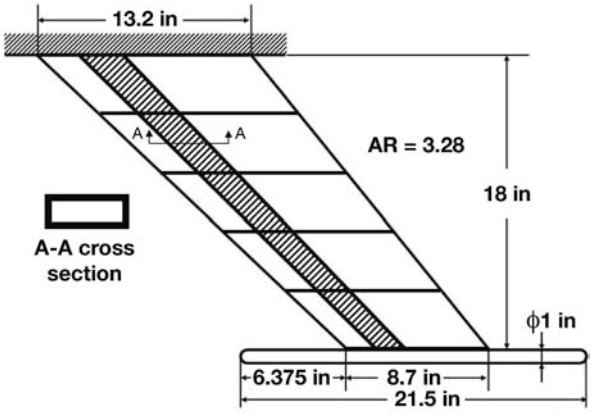

Fig. 5. Exploded view of the ATW2.

Fig. 6. The PONTOS photogrammetry optical measuring system.

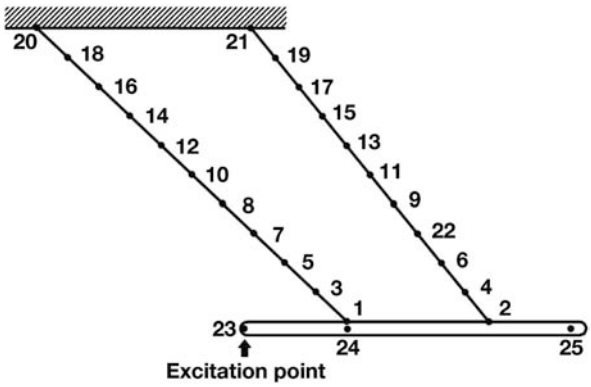

Fig. 7. GVT sensor and excitation locations.

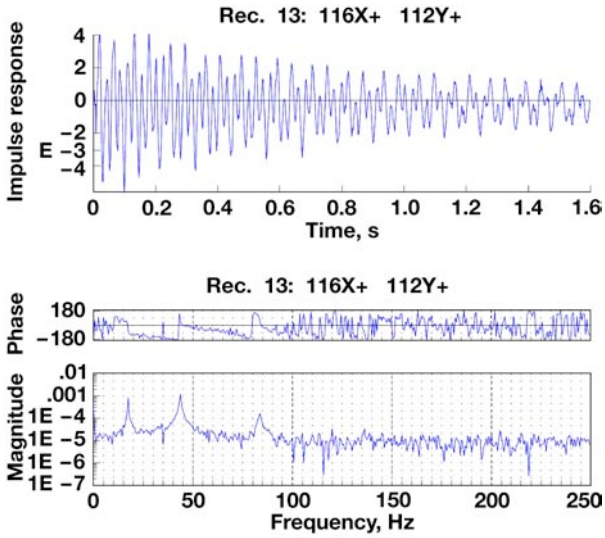

Fig. 8. Typical time history and frequency response GVT results for the ATW2.

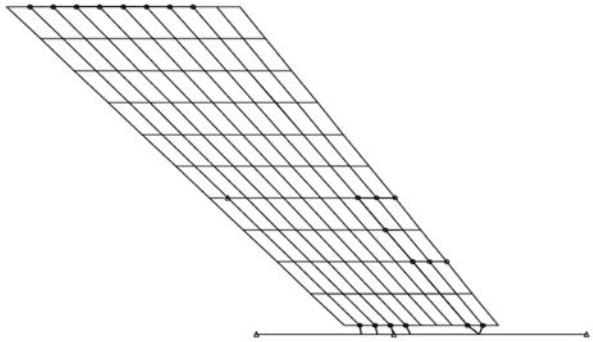

Fig. 9. MSC/NASTRAN finite element model.

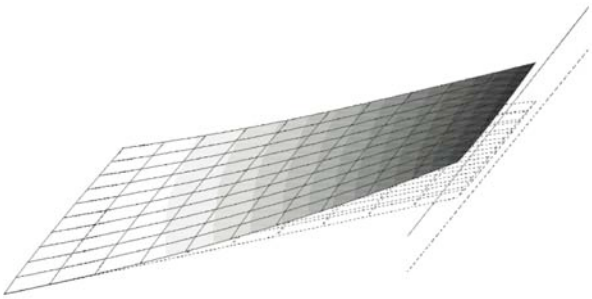

Fig. 10a. Mode 1 (1st bending): 17.60 Hz.

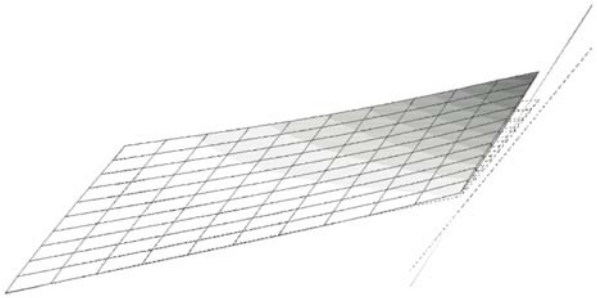

Fig. 10b. Mode 2 (1st torsion): 23.26 Hz.

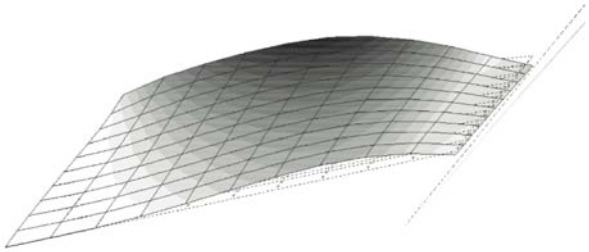

Fig. 10c. Mode 3 (2nd bending): 93.99 Hz.

Fig. 10. Full model mode shapes before tuning.

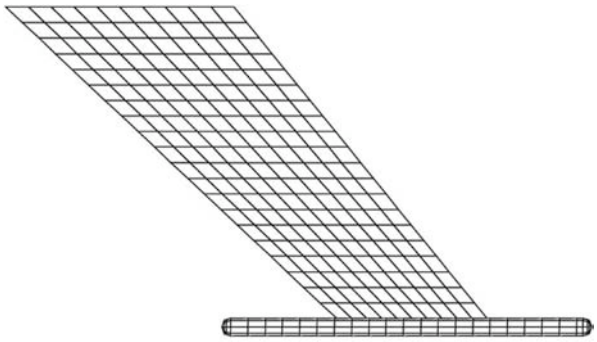

Fig. 11. ZAERO unsteady aerodynamic model.

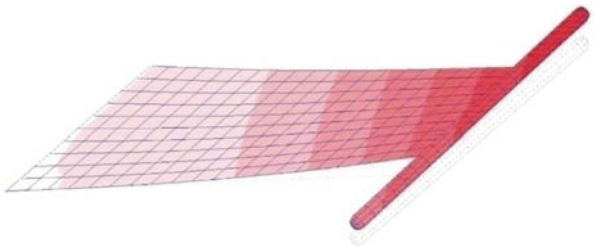

Fig. 12a. Splined mode 1.

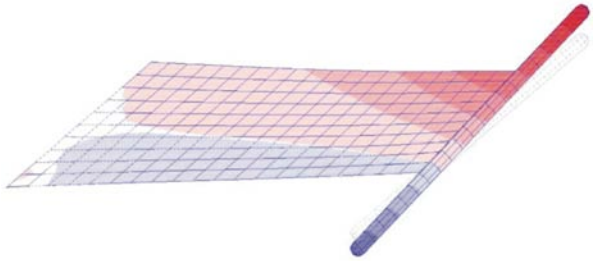

Fig. 12b. Splined mode 2.

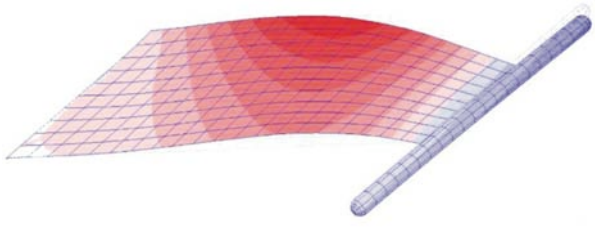

Fig. 12c. Splined mode 3.

Fig. 12. Splined mode shapes on unsteady aerodynamic model.

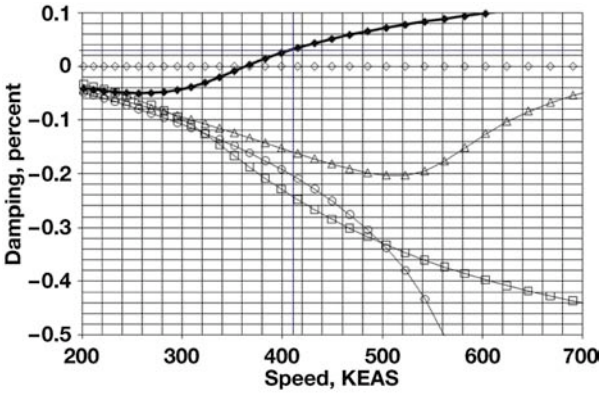

Fig. 13a. V-g plots.

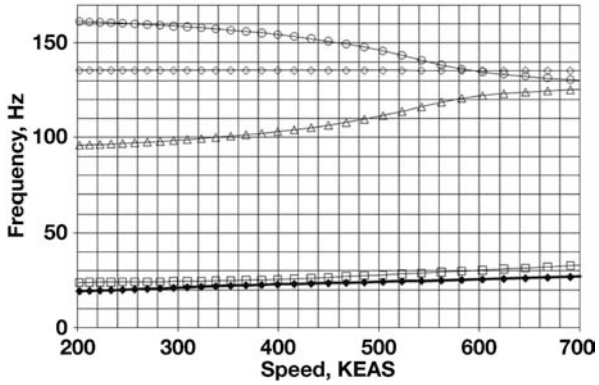

Fig. 13b. V-w plots.

Fig. 13. V-g and V-w plots for the ATW2 at Mach 0.82 before model tuning (plot the first 5 modes).

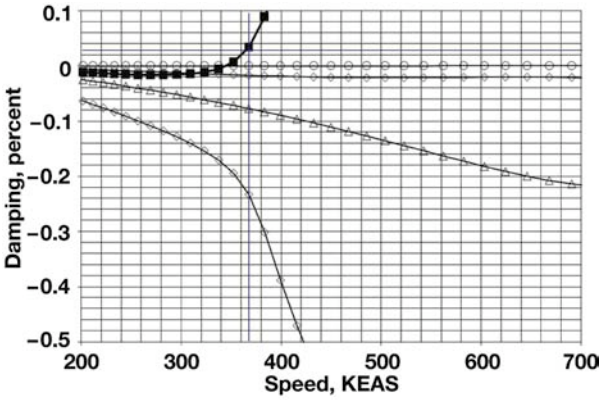

Fig. 14a. V-g plots.

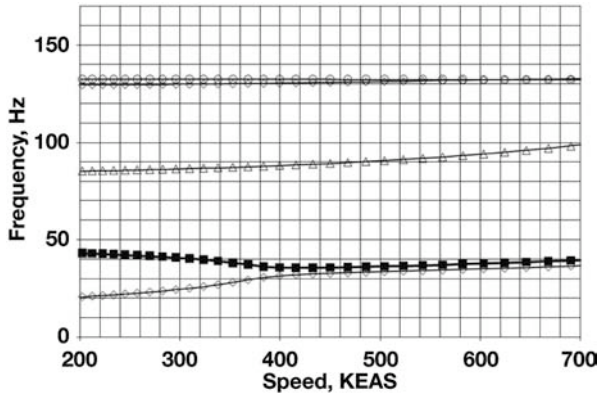

Fig. 14b. V-w plots.

Fig. 14. V-g and V-w plots for the ATW2 at Mach 0.82 after model tuning (plot the first 5 modes).

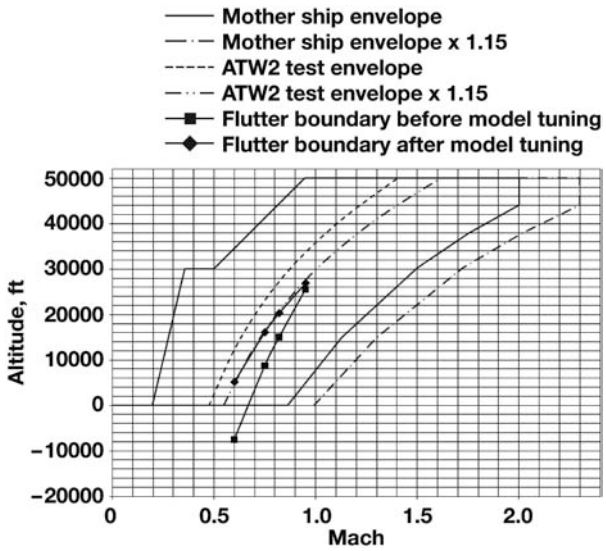

Fig. 15. Flutter boundary before and after model tuning.

Copyright Statement